

# How to design a 2D active grid for dynamic inflow modulation

Tom T. B. Wester<sup>1</sup> · Johannes Krauss<sup>1</sup> · Lars Neuhaus<sup>1</sup> · Agnieszka Hölling<sup>1</sup> · Gerd Gülker<sup>1</sup> · Michael Hölling<sup>1</sup> · Joachim Peinke<sup>1</sup>

**Abstract** Wind turbines operate under very dynamic conditions in the atmospheric boundary layer. Rapid changes of the angle of the incoming flow are caused by so called extreme conditions, either directly by changes of the wind direction or indirectly by gust induced changes of the angle for a rotating blade of the wind turbine. This dynamic changes lead frequently to the aerodynamic phenomenon of dynamic stall, which is known to generate a massive lift overshoot and therefore an increase of loads acting on the wind turbine.

In this study an experimental approach to modulate the inflow in a wind tunnel in a two-dimensional manner will be presented. For a complete characterization of the possibilities of the so-called 2D active grid, it is investigated with different modifications of the used shafts. In addition to the hardware alterations, the influence of the dynamic motion of the grid is also extensively investigated. The benefit of a 2D active grid upstream of the airfoil is the possibility to induce dynamic phenomena without the need to dynamically pitch the airfoil itself. This allows for simultaneous measurements of the flow field around airfoils with temporally high resolving particle image velocimetry (PIV) and load cells. Disturbing effects, such as those caused by the inertia of a moving airfoil, can be avoided. In addition to this dynamic changes in the angle of attack, it will be shown that the 2D active grid design enables to generate fast velocity fluctuations to mimic longitudinal inflow variations. These two features can be combined, resulting in angle of attack and velocity changes on small time scales with any phase shift between them to imitate different inflow situations such as yaw effects.

**Keywords** Active Grid · Flow Modulation · Dynamic Stall · Wind Tunnel · PIV

## 1 Motivation

For rapidly changing inflow conditions the aerodynamics of all kind of objects becomes challenging. An actual example are wind turbines operating in the atmospheric boundary layer, which are often subject to rapid inflow variations. Such so-called extreme conditions can manifest themselves as gusts or sudden shifts in direction of the incoming wind field. For the rotating blade these alterations mean a change in the angle of incidence (AoI) resulting in effects like dynamic stall. Dynamic stall causes dynamic loads on the blade, which are passed from there towards the drive train and the power electronics of the wind turbine, resulting in an increase of fatigue and therefore in a reduction of the lifetime of the whole turbine [1].

The aerodynamic phenomenon of dynamic stall was first observed nearly a century ago during two dimensional measurements of a Göttingen 459 profile [2]. Since then, the phenomenon has received more attention in the field of helicopter aerodynamics [3, 4], where the dynamic stall is caused by the rapidly changing relative speed of the rotor moving forward or backward compared to the flight direction of the helicopter and the periodic pitching of the rotor. On wind turbine rotors, the dynamic stall is mainly caused by the changing inflow rather than a pitching of the blades. Studies comparing the effect of a changing inflow and a pitching blade indicate a similar behavior of the flow around the airfoil [5, 6]. Based on these findings, it makes sense to turn the flow instead of the wing. This simplifies particle image velocimetry (PIV) and force measurements on the airfoil, since the force signals are not subject to

<sup>1</sup>ForWind, Institute of Physics, University of Oldenburg  
Küppersweg 70  
Tel.: +49-441-7985023  
Fax: +49-441-7985099  
E-mail: tom.wester@uni-oldenburg.de

any additional inertia. Furthermore, the light sheet for PIV measurements does not need to be adjusted individually, but can remain unchanged for different AoI amplitudes at fixed geometric angle of attack (AoA)  $\alpha$  of the airfoil.

The influence of incoming gusts on airfoils was already modeled in the early 20th century by Sears [7]. He used the thin-airfoil theory and a distribution of vortices along the camber of the airfoil to describe the gust airfoil interaction. Later this theory was expanded with second order models of Goldstein and Atassi [8] and Atassi himself [9]. With a new experimental approach, the results of Sears and Atassi were experimentally confirmed when a wind tunnel with active grid was used, for which the incident wind direction could be changed while a profile could remain in a fixed position [10]. Previous studies under comparable experimental conditions showed an ambiguity of both theories [11] and it was long unclear why this ambiguity occurred.

The main difference between [10] and [11] was the used active grid for inflow generation. [11] used an active grid which was developed to generate realistic turbulent inflow fields [12,13]. However, subsequent studies have shown that the active grid generates three-dimensional flows due to the geometric shape of the flaps [14]. In airfoil experiments this leads to a variation of the inflow along the span of the airfoil. In Fig. 1(a) the AoI ( $\phi$ ) based on the results shown in [14] is plotted over the by the period length  $T$  normalized time  $t$ . Depending on wind tunnel velocity and grid amplitude, the phase shift of the angle of attack along the span can vary by up to  $\varphi = 180^\circ$  along a single flap. In Fig. 1(b) the phase shift between the flap tip and the rod of the shaft in the middle between two flaps is  $\varphi = 108^\circ$ . The figure also implies that the phase shift and the induced structures are very stable, since the measurement takes place ten mesh sizes behind the grid and the sinusoidal variation of the inflow can still be seen very well. The shown flow structure is also repeated in space, because each shaft of the grid consist of seven flaps. The influence of the three-dimensionality of the generated inflow is often not desired in 2D airfoil experiments. For this reason the 2D active grid was designed. This was used in [10] to create well defined inflow conditions for the validation of the Sears and Atassi theories.

In the present study further possible applications of this 2D active grid will be presented. While in [15] two guiding vanes and in [16] a pitching and plunging airfoil was used to vary the AoI, this study will show further possibilities by varying the number and geometry of the used shafts. The presented 2D active grid can be equipped with up to nine individual moving shafts, resulting in a high flexibility in inflow generation. In addition to the

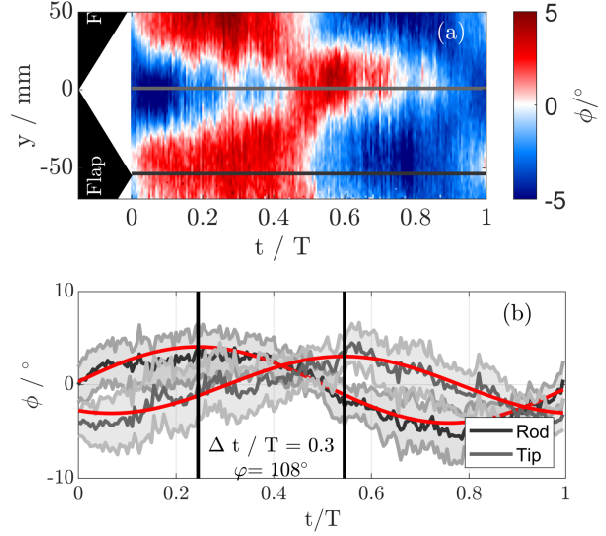


**Fig. 1** (a) Phase averaged PIV measurements of angle of incidence (AoI) change behind the active grid over the by period length  $T$  normalized time based on [14]. Also the implied position of the active grid flaps 1.1m upstream is shown. (b) Time series of the angle of incidence behind the active grid extracted from the shown PIV data at a position behind the rod and a position behind the tip indicated by horizontal lines in (a). Also plotted are sinusoidal fits and the phase shift between the time series.

AoI variation, some of the shafts can be used for example to vary the blockage to mimic longitudinal gusts. Such velocity changes are usually achieved by modulating the fan speed, but are limited by the reaction time of the entire tunnel, which is usually in the order of a few seconds. Another possibility is the use of so-called louvers downstream of the airfoil to increase the blockage, resulting in somewhat faster changes up to 3.2Hz [17]. Another device which increases the blockage upstream of the airfoil was introduced in [18] with frequencies up to 0.4Hz. By using the new developed 2D active grid, this can be reduced to time scales well below one second. Since not all shafts are needed for blocking, the grid also allows combinations between longitudinal gusts and AoI variations.

The paper is structured as follows. First the used experimental setup is presented in Sec. 2. This includes the wind tunnel in Sec. 2.1 and the new 2D active grid in Sec. 2.2 with its different configurations and shaft shapes. In the following, the different possible inflows are discussed in Sec. 3. In a first step the two-dimensionality of the generated flow field is shown in Sec. 3.1. Then in Sec. 3.2 the achievable inflows are compared based on the grid configuration. In Sec. 3.3 the possible longitudinal gusts are presented, followed by the combination of AoI and velocity fluctuations in

Sec. 3.4. An exemplarily application is shown in Sec. 4, where a PIV measurement of a profile subject to such AoI variation is shown. Finally, Sec. 5 concludes the paper.

## 2 Experimental setup

### 2.1 Wind tunnel

The following experiments are all performed in a wind tunnel using a closed test section. A sketch of the tunnel is shown in Fig. 2. It is a closed loop wind tunnel of Göttingen-type with a maximal speed of 50m/s. The closed test section has a cross section of  $(0.8 \times 1.0)\text{m}^2$  ( $h \times w$ ) and a length of 2.6m. The side walls as well as the top and bottom of the closed test section are made of acrylic glass walls to allow full optical access for measurements with Laser Doppler Anemometer (LDA) or PIV. The figure also shows the coordinate system used for the following results.

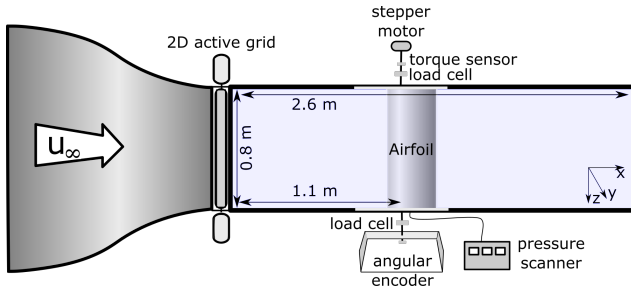


**Fig. 2** Used experimental setup. Inflow is coming from left and passes the 2D active grid, which is mounted at the nozzle. The flow travels then downstream towards the airfoil which is mounted in the middle of the wind tunnel.

1.1m downstream of the outlet an airfoil can be mounted into the test section. The airfoil is mounted in such a way that it can be rotated around the quarter point by a stepper motor which is on top of the test section. An angle encoder on the underside of the profile axis is used to record the angular position of the profile during the measurements. For the aerodynamic characterization of airfoils, load cells and a torque sensor can be used, which measure at a temporal resolution of 1kHz. The load cells are mounted on top and bottom of the airfoil, the torque sensor only at the top.

To characterize the generated flow field of the 2D active grid, X-wire measurements are performed in the empty test section at the centerline position of the wind tunnel 1m downstream of the grid. A Dantec Streamline is used for the measurements together with the Dantec Streamware software. To capture the flow sufficiently

well, a sampling frequency of 20kHz with a low-pass frequency of 10kHz is chosen. The X-Wires are calibrated with a Dantec Flow Unit.

### 2.2 Active Grid

The 2D active grid uses up to nine vertical shafts with a span width of  $s_{shaft} = 800\text{mm}$ , a chord length  $c_{shaft}$  depending on the used type and  $g_{shaft} = 110\text{mm}$  spacing between each shaft. A technical drawing of the grid is shown in Fig. 3. Each of the shafts is equipped with a stepper motor that allows the shafts to be moved individually. The trajectory of the shafts is given to the stepper motors via NI motion control boards and movement protocols which contain the position for each time step. The time between different positions is 20 ms. A whole rotation of a shaft is divided into 51200 micro steps resulting in a theoretical step resolution of  $0.007^\circ/\text{step}$ . However, this step precision cannot be considered as motion accuracy. The angle  $\gamma$  between shaft and flow is defined like shown in Fig. 3 at the bottom. For an open grid the flap angle is defined as  $\gamma = 0^\circ$ . The minimum and maximum possible blockage of the grid is depending on the used shaft shapes, which are presented below.

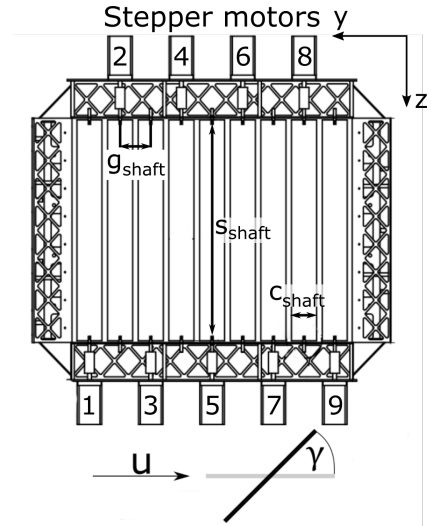


**Fig. 3** Technical drawing of the 2D active grid containing the stepper motors (1-9), the gauge of the shafts  $g_{shaft}$ , the span of the shafts  $s_{shaft}$  and the chord length of the shafts  $c_{shaft}$ . At the bottom the definition of flap angle  $\gamma$  is shown.

Three different shaft types (see Fig 4) are investigated for their impact on the resulting flow. The first shaft type I are flat plates with a chord length of  $c_{FP} = 90\text{mm}$  and a thickness of  $d_{FP} = 5\text{mm}$ . The pivot point of this shafts is in the middle to reduce inertia during the ro-

tation. Flat plates are chosen because they are very easy to manufacture and because they are geometrically closest to the diamond-shaped plates of the previously used active grid. The second shaft type **II** are 3D printed NACA0018 airfoils with a chord length of  $c_{\text{NACA0018}} = 71\text{mm}$  and a thickness of  $d_{\text{NACA0018}} = 12.8\text{mm}$ . For aerodynamic reasons the pivot point of those airfoils is at 25% of the chord length. This is also the reason for the reduction of chord length compared to the flat plates, otherwise the trailing edges of the shafts could collide. The shape is chosen to optimize the aerodynamic properties of the shafts. Especially when the angle  $\gamma$  becomes large, aerodynamic shapes show a more benign behavior than flat plates. The last shaft type **III** are 3D printed NACA0009 airfoils with a chord length of  $c_{\text{NACA0009}} = 180\text{mm}$  and a thickness of  $d_{\text{NACA0009}} = 16.2\text{mm}$ . Just like the NACA0018 airfoils, these are also rotated around the quarter point. This type of shafts is chosen in order to study the influence of the chord, whereby the aerodynamic shape of the shafts is also desired. All shafts have a span of 800mm to cover the complete height of the wind tunnel.

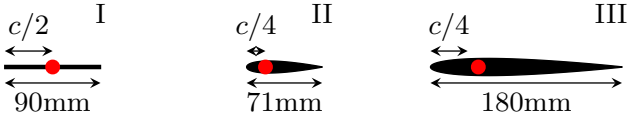


**Fig. 4** Used shafts for the 2D active grid. **I**: flat plates with a chord length of 90mm. **II**: NACA0018 airfoils with a chord length of 71mm. **III**: NACA0009 with a chord length of 180mm. The red dot indicates the pivot point.

In addition to the shaft types, the arrangement of these can also be varied. The Fig. 5 shows the configurations examined in this study. Configuration **i** shows the default setup with all nine shafts installed. This setup can be used for AoI modulations (see Sec. 3.2) by moving the shafts.

Another possibility is to use the outer shafts [1,2,8,9] marked in red to modulate the blockage induced by the grid up to 38%. The 38% refer to the case that the outer four shafts are completely closed ( $\gamma = 90^\circ$ ). The blockage can be individually adjusted according to the shaft angle. Depending on the aim the four or just two (Nr. [1,9]) of the shafts are used to do so.

The manipulation of the blockage can be used to generate longitudinal gusts (see Sec. 3.3). Since only the outer shafts are required for this, AoI variations can still be performed with the inner shafts. This is described in Sec. 3.4. Due to space limitations, only shaft types **I** and **II** can be considered for this configuration. In constellation **ii** the inner three shafts [4,5,6] are removed. This corresponds to the area in which the air-

foil to be examined later is located. The idea of this approach is to keep a very laminar flow in the middle of the measuring section, in which the influences of the shafts play no role. Only **I** and **II** are suitable for this configuration. Since the flow quality is the focus of this setup, in Sec. 3.2 only the results for the shafts **II** are shown. Due to the reduced number of shafts it is also not possible to generate the longitudinal gusts, as possible with setup **i**. Setup **i** and **ii** can be operated up to angular velocities of  $950^\circ/\text{s}$ .

The third setup **iii** uses only two shafts at the position [3,7]. This configuration is used with the NACA0009 airfoils **III** and is comparable to the setup used in [15], with the difference that only an open test section was used there. In this case the motivation is again to keep the wake of the shafts from the centerline. This setup can also be used to check whether the longer chord can lead to a more efficient deflection of the flow compared to many small shafts used in **ii**. The disadvantages here are also that no longitudinal variations are possible and the inertia of the shafts reduces the maximum rotation speed to  $400^\circ/\text{s}$ .

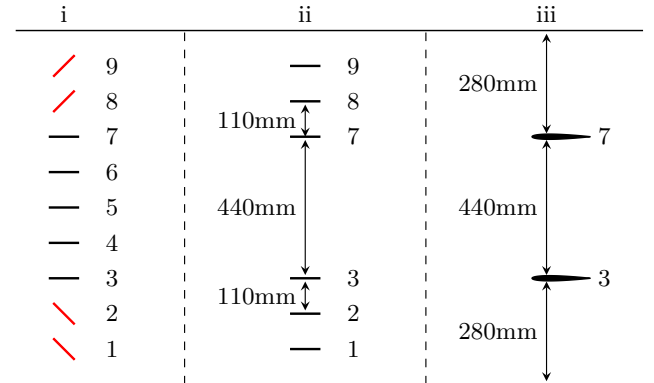


**Fig. 5** Shafts Setup of the 2D active grid as top view on the shafts. Figure **i** shows a setup with nine shafts, **ii** uses six shafts and in **iii** only two shafts of type NACA0009 are used.

### 3 Results of the inflow

This chapter is divided in four parts. The most essential and therefore first part is the verification of the two dimensionality of the generated flow field (Sec. 3.1). The homogeneity is checked both along the height of the wind tunnel and in horizontal direction. After this has been shown, the following three parts discuss the different possibilities resulting from the previously presented configurations. First the possible AoI variants and the influence of different shaft types are discussed (Sec. 3.2). It is then shown that also longitudinal gusts can be gen-

erated (Sec. 3.3) before it is shown in the last part that a combination of longitudinal gusts and AoI variations with arbitrary phase shifts is also possible (Sec. 3.4). In order to characterize the grid the dimensionless reduced frequency

$$k = \frac{\pi c f}{u_\infty} \quad (1)$$

[19] is used in all presented results.  $c$  denotes hereby the chord length of the considered object (active grid shaft or airfoil to be examined),  $u_\infty$  the inflow velocity given by the wind tunnel speed and  $f$  the frequency of the shaft movement or comparable the frequency of the modulated AoI. In general  $k$  indicates the sweep time of the flow along the object surface. The smaller  $k$  is, the longer the sweep time and thus the smaller the dynamics. Therefore, the reduced frequency is ideal for the analysis, as it makes it easy to compare the different used wind speeds and chord lengths of the shafts. Besides the reduced frequency  $k_{Grid}$  related to the grid shafts, the resulting reduced frequency  $k_{Airfoil}$  for an airfoil with a chord of  $c_{Airfoil} = 180\text{mm}$  is always displayed.

### 3.1 Two-dimensionality of the generated flow

The main motivation for building the 2D active grid is to get rid of the three-dimensionality of the previously used active grid. This three-dimensionality can lead to different flow phenomena happening on the airfoil which are not desired in 2D experiments. For this reason, the two-dimensionality of the 2D active grid is first checked by hot-wire measurements. For this purpose, an X-wire is positioned on the center line of the measuring section. A second X-wire is then moved step by step in z-direction towards the channel bottom with the help of a traverse. Since the shafts of the grid are symmetrical along the span, no traversing upwards is performed. A distance between the measuring points of 5cm is chosen. For these comparison measurements the setup **II/i** is chosen and operated with a reduced frequency of  $k_{Grid} \approx 0.1$  with an amplitude of  $\hat{\gamma} = 7.5^\circ$ . The results of the measurement are shown in Fig. 6. Black represents the centerline measurement and the lighter shades of grey represent the traversed X-wire measurements. The figure represents the resulting change in AoI, with the results of the respective positions shifted along the y-axis for better comparison. The data shown are phase averaged data together with the standard deviation of the phase averaging.

To check the homogeneity in the horizontal direction PIV measurements are performed. Fig. 7 shows the AoI

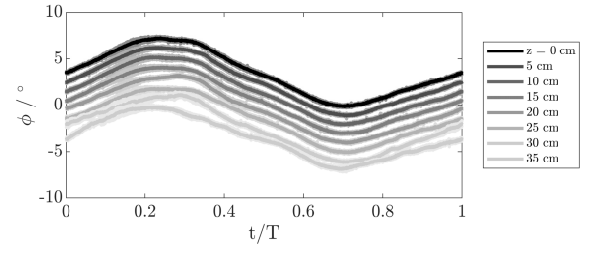


**Fig. 6** Check of the two-dimensionality of the flow generated by the grid along the z-direction. The measured data are shifted against each other along y for better representation. The measurements are performed with setup **II/i** at  $k_{Grid} \approx 0.1$  and  $\gamma = \pm 7.5^\circ$  amplitude.

at the airfoil position at the centerline height along the y-direction over time normalized by the period length  $T$  of the sinusoidal shaft motion. As can be seen, the AoI changes run very homogeneously through the channel.

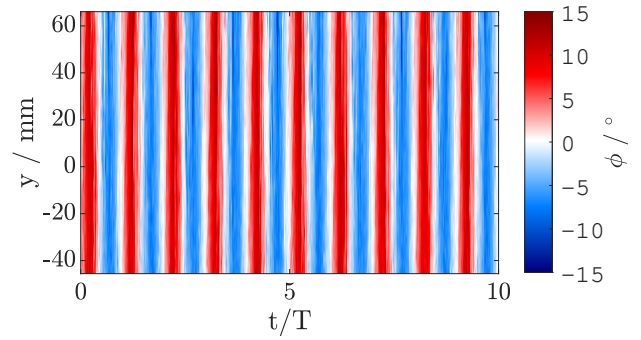


**Fig. 7** Temporal evolution of the angle of incidence in the wind tunnel in horizontal y-direction.

Both data clearly show that the flow does not change along the span of the shafts or the horizontal direction. The shape and also the standard deviation of the AoI curves along the z and y direction is identical. The results also show that there is no phase shift between the different measuring points. This is a clear indication that the 2D active grid setup allows a purely two-dimensional flow to be generated.

### 3.2 Angle of incidence modulation

In this section different setups will be discussed regarding the possible AoI variations. Mainly three properties of the setups shall be considered: 1. Phase averaged time signal of the AoI. 2. Resulting AoI magnitude  $\hat{\phi}$  as a function of the reduced frequency of the grid  $k_{Grid}$ . 3. Resulting AoI magnitude  $\hat{\phi}$  as a function of the shaft amplitude  $\hat{\gamma}$ . A comparison of the properties is shown in Fig. 8 for the setups **I/i**, **II/i**, **II/ii** and **III/iii**. The



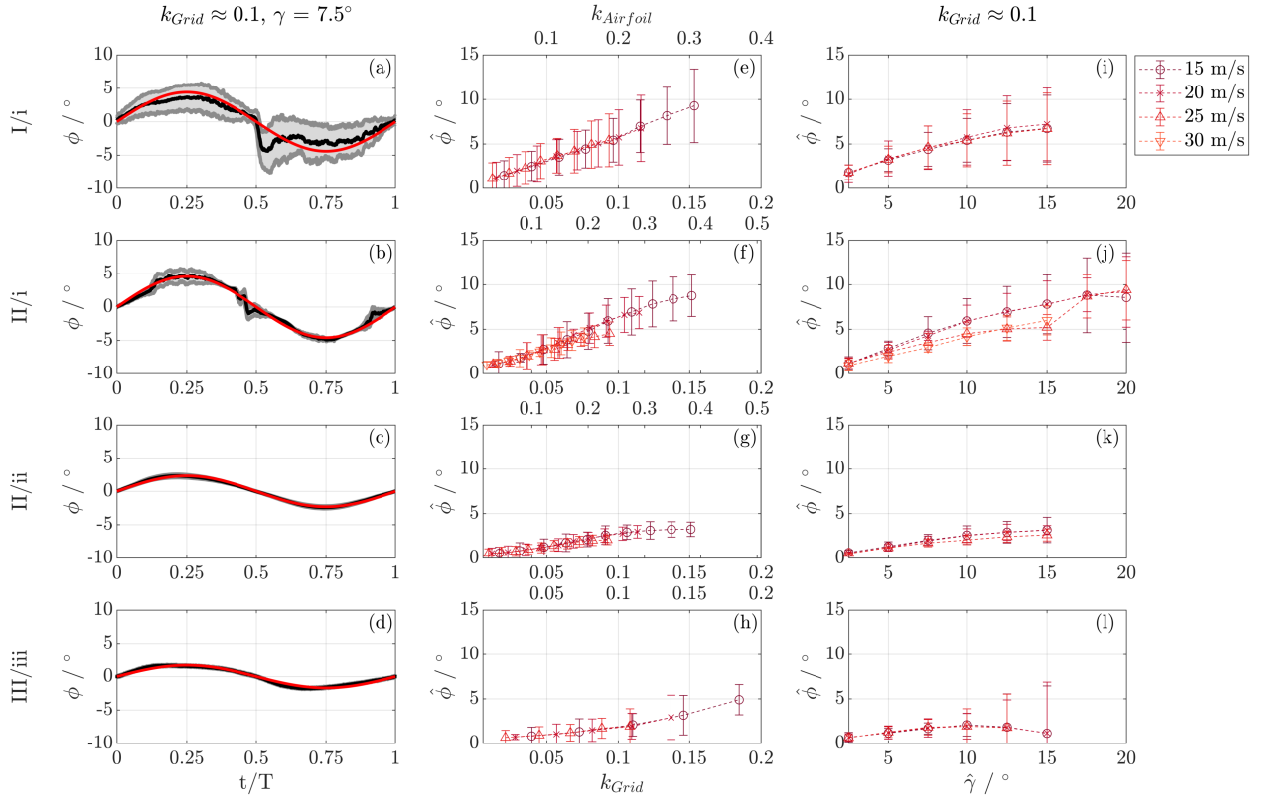


**Fig. 8** Comparison of different setups. The first column shows the time signal for a grid movement of  $\hat{\gamma} = 7.5^\circ$  at a reduced frequency of  $k_{Grid} \approx 0.1$ . Second column shows the produced AoI magnitude  $\hat{\phi}$  for different reduced frequencies  $k_{Grid}$  of the grid types. In addition the upper x-axis shows the resulting reduced frequency  $k_{Airfoil}$  for an airfoil of  $c = 0.18m$ . The third column shows the resulting AoI magnitudes for different shaft amplitudes  $\hat{\gamma}$  at fixed reduced frequency of  $k_{Grid} \approx 0.1$ .

data are generated using sinusoidal movements of the grid shafts with different frequencies  $f$  and amplitudes  $\hat{\gamma}$  of the grid. The parameters are listed in table 1.

**Table 1** Parameter used during the characterization of the 2D active grid for different setups.

| Setup   | $f$ / Hz | $\Delta f$ / Hz | $\hat{\gamma}$ / $^\circ$ | $\Delta\hat{\gamma}$ / $^\circ$ |
|---------|----------|-----------------|---------------------------|---------------------------------|
| I/i     | 1-8      | 1               | 2.5-15                    | 2.5                             |
| II/i    | 1-10     | 1               | 2.5-20                    | 2.5                             |
| II/ii   | 1-10     | 1               | 2.5-15                    | 2.5                             |
| III/iii | 1-5      | 1               | 2.5-15                    | 2.5                             |

The first column of the Fig. 8 shows the phase averaged time signals in black with a sinusoidal fit in red. The grey regions around the line represent the standard deviation of the phase average and are therefore also an indicator of the fluctuations of the generated flow. The AoI  $\phi$  is plotted over  $t/T$ , where  $T$  is the period length of the sinusoidal movement.

In subplot (a) the resulting AoI for the flat plates **I** is shown. It can be seen, that the flow is redirected in a

sinusoidal way and the fit represents the trend of the flow direction. The standard deviation is quite large, which indicates a very high turbulence level of the generated flow. Furthermore a fast change in the AoI can be observed at  $t/T \approx 0.5$ . At this point two effects add up. First the passing of the shaft wake and second an aerodynamic effect of the shaft. For an angle of  $\gamma = 0^\circ$  the flow reattaches and therefore a very efficient redirection of the flow can be observed leading to this fast change.

Subplot (b) shows a comparable amplitude of the AoI variation for the NACA0018 **II** shafts. Compared to the flow from type **I** a significant reduction of standard deviation can be observed by looking at the standard deviation around the phase averaged data. Furthermore, the phase average shows nearly no deviation from the sinusoidal fit except for the maximum, minimum and the turning point. The increased standard deviation here can be explained by aerodynamic effects, which occur under dynamic movement. The increased standard deviation at maximum and minimum is induced by the separation happening on the shafts since they are turn-

ing with a lower angular velocity at these points and therefore a typical delayed separation known from dynamic stall occurs. The increase of the standard deviation at the turning point ( $\gamma = 0^\circ$ ,  $t/T \approx 0.5$ ) can be explained by the passing of the wake from the shafts, similar to the effect which was presented before.

While for setup **i** at  $t/T \approx 0.5$  a wake effect can be observed for both shaft types, it does not occur in setups **ii** and **iii** shown in the subplots Fig. 8 (c) and (d). For both configurations similar results can be observed. The AoI variation is very close to the sine fit and the standard deviation is very small. Comparing the amplitude with the configuration **i** an AoI variation that is smaller by a factor of more than two can be observed. Summarizing the time signals it can be said that with **i** very large AoI amplitudes can be generated, but a wake effect of the shafts on the centerline is also visible. Thus the changes of the AoI are accompanied with turbulent fluctuations, which may be desired for some investigations. Shaft type **I** is suitable for generating more turbulent flows, whereas shaft type **II** generates AoI variations with very low turbulence intensity. If a very laminar flow is desired and the amplitude is not decisive, then the setups **II/ii** and **III/iii**, which generate an almost perfect sine wave, are suitable.

The second column of Fig. 8 shows the dependence of the generated AoI magnitude  $\hat{\phi}$  on the reduced frequency of the grid  $k_{Grid}$  for the different setups and different flow velocities. The shown magnitudes result from sinusoidal fits like shown in the first column. To obtain the error bars, the fit is subtracted from the time series and the standard deviation of the remaining signal is calculated. This value thus indicates the deviation from the perfect sine. In the subplots (e)-(h) the lower x-axis represents the reduced frequency with respect to the chord of the shafts. The upper x-axis shows the reduced frequency for an airfoil with a chord length of 180mm. Subplot (e) shows a linear relation between the grid frequency and the generated inflow. The error bars also show that the deviations shown in subplot (a) also occur for other grid frequencies. Furthermore, the error bars increase with increasing reduced frequency. Subplot (f) shows comparable magnitudes  $\hat{\phi}$  for shaft type **II**, but smaller error bars. This is also in agreement with subplot (b). Here also an increase of the error with increasing frequency can be observed. The results for setup **ii** and **iii** shown in (g) and (h) show much smaller amplitudes. The deviation of the magnitudes compared to setup **i** is up to a factor of nearly three. In (g), comparatively small error bars can be observed. Here, a kind of plateau for  $k_{Grid} > 0.125$  can be seen, while in (h)  $\hat{\phi}$  shows a rise for these frequencies. In summary, the dependence of the generated magni-

tude on the reduced frequency shows a linear relationship over a large range. Also the error seems to grow linear for setup **i**, while it seems to remain rather constant for setups **ii** and **iii**. It is important to note here that the wind speed has no visible influence on the course of the curve. Furthermore, the collapsing curves show that the reduced frequency is a good choice for normalization. The results indicate that comparable flows can be generated by keeping  $k_{Grid}$  constant. A direct consequence is that a doubled reduced frequency with constant AoI can be generated for an airfoil by using shafts with half the chord length at constant wind speed.

Finally, the dependence of  $\hat{\phi}$  on the shaft amplitude  $\hat{\gamma}$  is examined in column three for a fixed reduced frequency of  $k \approx 0.1$  (Fig. 8 (i)-(l)). This  $k$  is chosen, because it is achievable for all setups. The shown curves show a saturation of the induced amplitudes for larger amplitudes  $\hat{\gamma}$ , which can be approximated with  $\hat{\phi}(\hat{\gamma}) = a \cdot \sqrt{\hat{\gamma}} + b$ , where  $a$  and  $b$  are independent fit parameters. It can also be seen that the error bars grow strongly with increasing amplitude. The shape of the curve is clearly due to the happening dynamic stall for larger  $\hat{\gamma}$  on the shafts. However, this does not lead to a significant drop in amplitude, but only to a less strong increase of  $\hat{\phi}$ . Furthermore, only a weak wind speed dependence can be seen. Just configuration **II/ii** shows a significant reduction of the amplitude at higher wind speeds, which ends abruptly for high amplitudes ( $\hat{\gamma} > 15^\circ$ ) and the curves again overlap. Here also a dynamic phenomenon seems to take over. In addition it should also be mentioned that for  $k \approx 0.15$ , amplitudes of up to  $\hat{\phi} = 15^\circ$  can be achieved using the setup **II/ii**.

In summary it can be said that even for very large shaft amplitudes an efficient redirection of the flow can be realized. The decreasing slope for larger  $\hat{\gamma}$  shows that dynamic effects at the grid shafts themselves play a role. In a next step the influence of not using all shafts in configuration **II/i** to redirect the flow is further investigated. For this purpose, the grid is controlled with a sinusoidal motion as before. However, the outer shafts are left at the  $\gamma = 0^\circ$  position. Fig. 9 shows the resulting magnitudes  $\hat{\phi}$  for a wind speed of 15m/s. (a) represents the the magnitude relative to the grid frequency and (b) the magnitude relative to the shaft amplitude. The results for nine shafts are the same as shown in Fig 8(f) and (j). Seven shafts means that shafts [1,9] are not moving, for five shafts [1,2,8,9] are not moving. The curves show that the outer shafts do not have a great impact on the generated flow. The amplitude decreases only slightly when using fewer shafts. The shape of the curves also remains completely unchanged.

In summary, it can be said that the shaft arrangement determines the possible magnitudes. It could also be

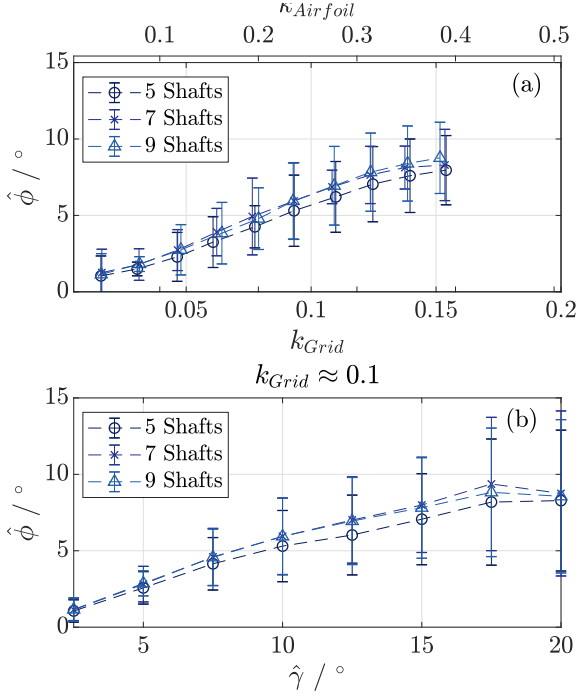


**Fig. 9** Variation of the number of used shafts in setup **II/i** at fixed wind speed of 15m/s. (a) shows the produced AoI magnitude  $\hat{\phi}$  for different reduced frequencies  $k_{Grid}$  for five, seven or nine shafts. In addition the upper x-axis shows the resulting reduced frequency  $k_{Airfoil}$  for an airfoil of  $c = 0.18m$ . (b) shows the resulting AoI magnitudes for different shaft amplitudes  $\hat{\gamma}$  at fixed reduced frequency of  $k_{Grid} \approx 0.1$ .

shown that the outer shafts do not have a great impact on the generated AoI magnitude at the centerline. Furthermore, the shape of the shafts can be used to adjust the quality of the flow. Depending if a underlying turbulence level is desired or not. Likewise, a perfectly sinusoidal AoI can be generated by dispensing shafts on the centerline. The frequency and amplitude study showed that the wind speed has nearly no influence on the generated  $\hat{\phi}$ , which grows monotonic for all cases over a broad region of frequencies. The only influence of the wind speed can be observed for the configuration **II/i**, if the amplitude  $\hat{\gamma}$  of the grid is strongly varied.

### 3.3 Velocity modulation

After it has been shown that the grid allows fast and large changes of the angle of incidence in different turbulence levels and over a wide range of velocities, the following chapter investigates how strong longitudinal gusts can be imposed. Until now there have been different approaches to vary the inflow velocity by placing the different blockage devices downstream of the test section. With this velocity modulations up to 3.2Hz could be realized [17]. Using the 2D active grid the velocity

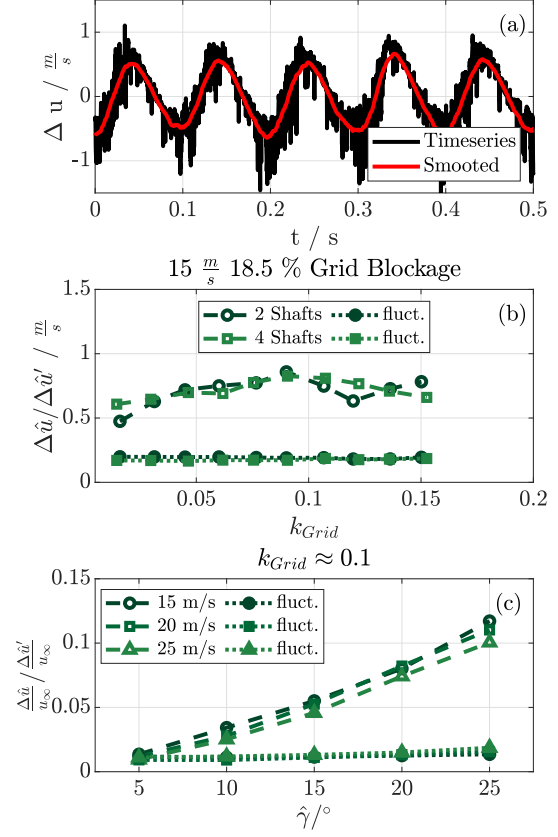


**Fig. 10** Overview over the longitudinal gusts. (a) shows a time series of velocity fluctuations induced by increasing the blockage using outer shafts in setup **II/i**. The reduced frequency is  $k_{Grid} \approx 0.1$  at an inflow velocity of 20m/s. The red line shows the over 500 samples smoothed time series. (b) shows possible velocity variations for a fixed blockage ratio of 18.5% for grid with setup **II/i**. The filled symbols represent the standard deviation around the modulated flow. (c) shows possible normalized velocity fluctuations for reduced frequency of  $k_{Grid} \approx 0.1$  for grid setup **II/i** using the four outer shafts. The filled symbols represent the standard deviation around the modulated flow.

modulations up to 10Hz can be imposed upstream of the airfoil by using the outer shafts [1,2,8,9]. To have a high flexibility in changing the blockage, configuration **III/iii** can not be used due to the few shafts. Since the two or four outer shafts are used to change the blockage, configuration **ii** is also excluded from the selection, since the two remaining shafts can no longer be used to achieve variations in AoI. For this reason **II/i** is chosen for the following experiments.

The inner shafts remain unchanged at the  $\gamma = 0^\circ$  position, while the outer shafts perform a sinusoidal movement. The motion starts at half of the desired amplitude with the shafts trailing edge pointing towards the



wind tunnel walls and is then moved between  $\gamma = 0^\circ$  and the amplitude  $\hat{\gamma}$  to increase the blockage of the grid. An exemplary time series resulting from such a motion is given in Fig. 10(a) where four outer shafts are used to generate such a gust. The amplitude of the movement is  $\pm 10^\circ$  resulting in a velocity modulation of  $\Delta u = \pm 0.6 \text{ m/s}$  at an inflow velocity of  $20 \text{ m/s}$ . The shafts move with a frequency of  $f_{Grid} = 10 \text{ Hz}$  corresponding to a reduced frequency of  $k_{Grid} \approx 0.1$ . The time series shows a periodic behavior, but the shape of the raw signal is not perfect sinusoidal. This is a problem that arises due to the inertia of the flow itself. By increasing the blockage a speed up is very easy to achieve, but when the grid reopens the flow does not recover immediately. This is the reason for the increased fluctuations in the valleys of the signal.

In the Fig. 10(b) a comparison of the achievable velocity modulation for a maximal blockage of  $18.5\%$  is shown. The difference between the two colors is that for one case only the two shafts ([1,9]) are used, whereas for the other one the mentioned four shafts ([1,2,7,9]) are used. The hollow points in the plot represent the amplitude of the velocity modulation  $\Delta \hat{u}$  from a sinusoidal fit. The filled points represent the fluctuations  $\Delta \hat{u}'$  around the velocity modulation. The fluctuations are calculated by subtracting the smoothed curve (see Fig. 10(a) red line) from the time series and calculating the standard deviation of the remaining signal. The amplitude of the velocity modulation  $\Delta \hat{u}$  and the fluctuations  $\Delta \hat{u}'$  seem to be independent from the reduced grid frequency  $k_{Grid}$ , which is given as x-axis. Furthermore, this plot emphasizes that the amplitude  $\hat{u}$  is also just depending on the blockage and not on the number of axis which are used for generating the blockage.

Fig. 10(c) shows the induced velocity modulation for three different inflow velocities over the amplitude of the shafts  $\hat{\gamma}$ . The resulting velocity modulations are normalized by the inflow velocity  $u_\infty$ , to compare the plots. The filled symbols represent again the fluctuations around the modulation  $\Delta \hat{u}'$ . All data show a similar behavior which means, that the resulting velocity modulation is also not depending on the inflow velocity, but is depending on the induced blockage. This is represented by the monotonic increase of the velocity modulation when the amplitude of the shafts is also increased. Furthermore, it should be mentioned that the fluctuations  $\Delta \hat{u}'$  are constant for the whole investigated range.

In summary Fig. 10(b) and 10(c) show, that a broad range of velocity fluctuations is possible and those are just depending on the blockage of the grid. Neither the frequency of the grid nor the inflow velocity have an impact on the resulting fluctuations. Also the number

of shafts that are used are not critical for the generation of velocity fluctuations.

### 3.4 Combination of AoI and velocity modulation

Next it will be shown how angle of incidence and velocity modulations can be combined using the 2D active grid. Fig 11(a) shows the variation of the inflow velocity  $u$  in green on the left y-axis and the AoI fluctuations in red on the right y-axis. The variations are a superposition of the fluctuations presented in the previous chapters. It can be seen that the fluctuations are in phase, i.e. the angle of incidence is maximum when the velocity reaches its maximum.

The opposite phase can be seen in Fig. 11(b), where the angle of incidence is  $180^\circ$  ahead of the velocity fluctuation. This emphasizes the flexibility of this setup. The phase shift between the angle of incidence and velocity fluctuation can be varied completely arbitrarily.

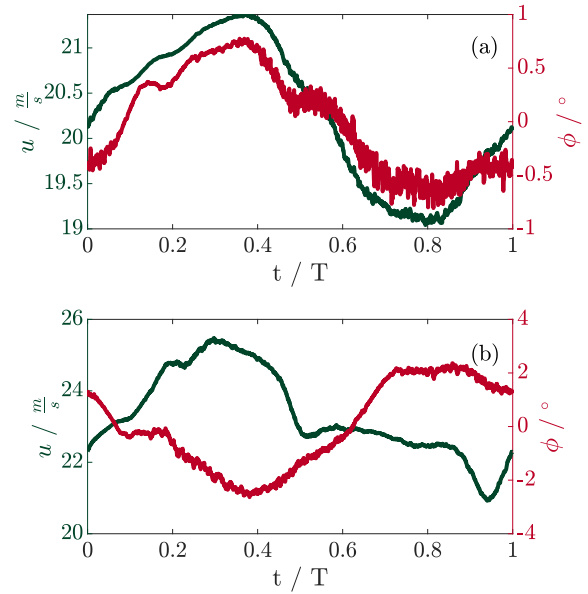


**Fig. 11** (a) example of simultaneous in phase variations of inflow velocity  $u$  and angle of incidence  $\phi$ . (b) example of simultaneous out of phase variations of inflow velocity  $u$  and angle of incidence  $\phi$ .

Summarizing chapter 3 it could be shown that the new 2D active grid generates a 2D inflow field like desired. Subsequently, the 2D active grid is extensively characterized, whereby the influence of different shafts on the generated angles of incidence is shown. Furthermore, the influence of the number of axes on the AoI generation is examined. In addition to the AoI variations, the

possibilities of varying the speed in the form of longitudinal gusts are also investigated. It was demonstrated that very fast speed changes can be realized with the grid. In the last section it is shown that the AoI variations can be combined with the velocity modulations in any phase.

#### 4 Application of 2D grid for airfoil measurements

In this chapter an exemplary experiment with a Clark Y-profile with a chord length of  $c_{Airfoil} = 180\text{mm}$  is presented, which experiences dynamic changes of the flow through the 2D active grid. For this purpose, the experiment setup shown in 2.1 with the active grid presented before is used. Other measurements using this setup were presented in [20] and [21].

For this experiment a pure AoI variation is produced by the configuration **I/i** generating an inflow amplitude of  $\hat{\phi} = \pm 6^\circ$ . The airfoil is placed in the middle of the test section, the dynamic forces acting on the airfoil are measured using the load cells. The airfoil is turned to a static geometric angle of attack of  $\alpha = 8^\circ$  which leads together with the inflow to a dynamic inflow cycle of  $\alpha_{Inflow} \in [2, 14]^\circ$ . Since the airfoil is not turned, no inertial forces occur and therefore no dynamic corrections of the measured forces are necessary. The Fig. 12 shows the static polar of the airfoil in black, which was measured beforehand under laminar conditions. In addition to the static lift, also the dynamic lift measured by load cells is plotted in red. The sinusoidal inflow has a frequency of  $f_{Inflow} = 8\text{Hz}$  resulting in a reduced frequency of  $k_{Airfoil} = 0.3$ , which is a highly unsteady inflow condition. This is also represented by the typical dynamic stall loop, which shows the typical lift overshoot for increasing  $AoA$ , a sudden drop of lift when the angle does not increase further and the undershoot of lift during the decreasing angle of attack until the minimum is reached and the cycle starts again.

The big advantage of this experimental approach presented here is that it allows a quite easy way to perform temporal and spatial resolved stereoscopic PIV measurements with a sampling frequency of 500Hz (see also [20]) together with force measurements at 1kHz. This is only possible, because the airfoil is static and therefore the light sheet and cameras do not need to be adjusted for this large angular range. This setup also enables a measurement which is not phase locked, but fully time resolved. Snapshots of the PIV measurement are shown in Fig. 13. This flow field is taken from the same measurement, which resulted in the dynamic stall cycle shown in Fig. 12. The snapshots show the flow around the airfoil at different angle of attack. A typical

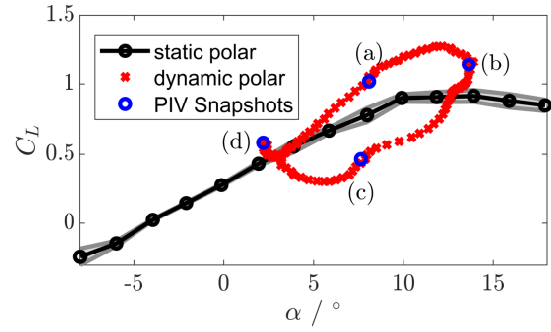


**Fig. 12** Measured forces of an airfoil for the static case (black) and the dynamic case (red) over the angle of attack  $\alpha$ . The blue circles indicate the positions of the PIV snapshots shown below on the dynamic stall cycle.

behavior of the flow can be observed since the flow stays attached during the rising angle of attack in subplot (a), shows a flow separation at the trailing edge at the maximum angle in (b), reattaches when the angle of attack decreases again in (c) and is also attached at the minimum angle in (d). For the separation in (b) the area is limited to the trailing edge, the point where the flow separates can also be located and is plotted as a red dot into the picture.

#### 5 Conclusion

In this study a new type of active grid is presented. The special feature about this 2D active grid is that it enables the generation of highly dynamic two-dimensional flows. In addition to proving that the new design is capable of generating a purely 2D flow, this study also tests different configurations of the grid for their flow physical properties.

The main focus of the experiments is on the producible angle of incidence amplitude  $\hat{\phi}$ . The analysis of the different configurations and parameters of the shaft motion shows that the quality of the flow can be changed by the shaft type. While flat plates (**I**) can produce a very turbulent flow, aerodynamically shaped shafts (**II-III**) can produce very clean AoI variations. It is also demonstrated that the wind speed has little influence on the generated amplitudes. The reduced frequency at the grid shafts seems to be the most important key figure, since the curves collapse for different chords and wind speeds if the results are normalized by this relation. Hereby it is possible to adapt the grid to the respective needs by varying the shaft chord and the grid frequency.

Besides the AoI variations it is shown that the outer shafts have no strong influence on the modulation of the flow on the centerline. Therefore these shafts can

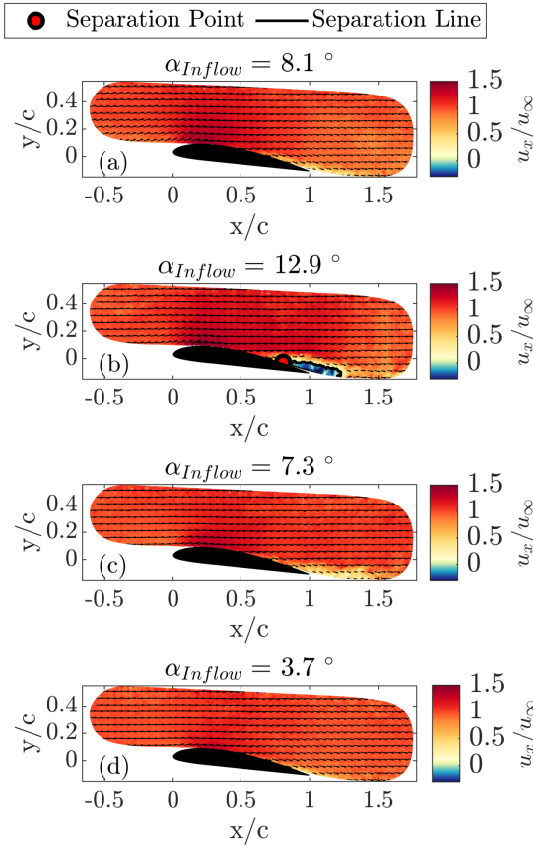


**Fig. 13** PIV Snapshot of the flow around an airfoil under dynamic inflow conditions.

be used to dynamically vary the blockage with the grid, thus rapidly changing the wind speed. It is found that the relative variation is not dependent on the wind speed, but only on the blockage itself. This applies to the frequency of the grid as well as to the grid amplitude. The findings on AoI and velocity variations are combined and it is shown that a simultaneous variation of both with any phase shift can be generated.

The shown possibilities to produce various inflow conditions are interesting in order to generate different flow situations in a wind tunnel and to investigate them under reproducible conditions. This includes for instance the typical flow situations like dynamic stall on a rotor blade of a wind turbine or the often occurring case of yaw misalignment. It is important to understand these effects in detail to incorporate this knowledge into the design of new wind turbines, so the lifetime of these turbines can be extended despite the extreme operating conditions that often occur.

Besides the application in the field of wind energy, such a kind of 2D active grid can also be used for other research areas where rapid inflow changes occur. Ex-

amples are helicopter aerodynamics as well as experiments on flying creatures, on whose wings dynamic effects typically play an important role. This emphasizes the broad applicability of the device presented here.

## 6 Acknowledgments

The present investigations were performed within the "Wind Turbine Load Control under Realistic Turbulent In-Flow Conditions" (PE 478/15-2 & HO 50272-2) project. The authors gratefully acknowledge the German Research Foundation (DFG) for funding the studies.

The authors also want to thank Lars Kröger and Piyush Singh for their support during the measurement campaigns.

## References

1. F. Spinato, P.J. Tavner, G. Van Bussel, E. Koutoulakos, *IET Renewable Power Generation* **3**(4), 387 (2009)
2. V.M. Kramer, Z. Flugtech. Motorluftschiff **23**, 185 (1932)
3. F.D. Harris, R.R. Prunyn, *Journal of the American Helicopter Society* **13**(2), 27 (1968)
4. J. Liiva, *Journal of Aircraft* **6**(1), 46 (1969)
5. K. Gharali, D.A. Johnson, *Applied Energy* **93**, 45 (2012)
6. D. Rival, C. Tropea, *Journal of Aircraft* **47**(1), 80 (2010)
7. W.R. Sears, A systematic presentation of the theory of thin airfoils in non-uniform motion. Ph.D. thesis, California Institute of Technology (1938)
8. M.E. Goldstein, H. Atassi, *Journal of Fluid Mechanics* **74**(4), 741 (1976)
9. H. Atassi, *Journal of Fluid Mechanics* **141**, 109 (1984)
10. N.J. Wei, J. Kissing, T.T.B. Wester, S. Wegt, K. Schiffmann, S. Jakirlic, M. Hölling, J. Peinke, C. Tropea, arXiv preprint arXiv:1811.10485 (2018)
11. U. Cordes, G. Kampers, T. Meißner, C. Tropea, J. Peinke, M. Hölling, *Journal of Fluid Mechanics* **811** (2017)
12. N. Reinke, Application, generation and analysis of turbulent flows. Ph.D. thesis, Universität Oldenburg (2017)
13. P. Knebel, A. Kittel, J. Peinke, *Experiments in Fluids* pp. 1–11 (2011). DOI 10.1007/s00348-011-1056-8
14. D. Traphan, T.T. Wester, M. Melius, J. Peinke, G. Gülker, R.B. Cal, arXiv preprint arXiv:2003.07840 (2020)
15. P.M. Lancelot, J. Sodja, N.P. Werter, R. De Breuker, *Advances in aircraft and spacecraft science* **4**(2), 125 (2017)
16. N.J. Wei, J. Kissing, C. Tropea, *Experiments in Fluids* **60**(11), 166 (2019)
17. D. Greenblatt, *AIAA Journal* pp. 1817–1830 (2016)
18. I. Neunaber, C. Braud, *Wind Energy Science* **5**(2), 759 (2020)
19. G.J. Leishman, *Principles of helicopter aerodynamics with CD extra* (Cambridge university press, 2006)
20. T.T.B. Wester, G. Kampers, G. Gülker, J. Peinke, U. Cordes, C. Tropea, M. Hölling, in *Journal of Physics: Conference Series*, vol. 1037 (IOP Publishing, 2018), vol. 1037, p. 072007
21. T.T.B. Wester, S. Bartholomay, D. Traphan, M. Hölling, J. Peinke, G. Gülker, (19th International Symposium on the Application of Laser and Imaging Techniques to Fluid Mechanics, 2018)